Artificial intelligence guided studies of van der Waals magnets

Trevor David Rhone,[1] Romakanta Bhattarai,[1] Haralambos Gavras,[1] Bethany Lusch,[2] Misha Salim,[2] Marios Mattheakis,[3] Daniel T. Larson,[3] Yoshiharu Krockenberger,[4] and Efthimios Kaxiras*[3]

[1]*Department of Physics, Applied Physics and Astronomy, Rensselaer Polytechnic Institute, 110 8th Street, Troy, NY 12180*
[2]*Argonne Leadership Computing Facility, Argonne National Laboratory, 9700 S. Cass Avenue, Lemont, IL 60439, USA*
[3]*Department of Physics, Harvard University, 17 Oxford St, Cambridge, MA 02138, USA.*
[4]*NTT Basic Research Laboratories, NTT Corporation, 3-1 Morinosato-Wakamiya, Atsugi, Kanagawa 243-0198, Japan*

A materials informatics framework to explore a large number of candidate van der Waals (vdW) materials is developed. In particular, in this study a large space of monolayer transition metal halides is investigated by combining high-throughput density functional theory calculations and artificial intelligence (AI) to accelerate the discovery of stable materials and the prediction of their magnetic properties. The formation energy is used as a proxy for chemical stability. Semi-supervised learning is harnessed to mitigate the challenges of sparsely labelled materials data in order to improve the performance of AI models. Our approach creates avenues for the rapid discovery of chemically stable vdW magnets by leveraging the ability of AI to recognize patterns in data, to learn mathematical representations of materials from data and to predict materials properties. Using this approach, previously unexplored vdW magnetic materials with potential applications in data storage and spintronics are identified.

I. INTRODUCTION

A. Magnetic ordering in reduced dimensions

Two-dimensional (2D) materials, also referred to as van der Waals (vdW) materials due to the weak interlayer forces, exhibit a range of interesting properties including superconductivity, topological insulating behavior and magnetic order [1]. There is an exigent need to identify 2D materials with properties suitable for advances in science and technological innovation. Traditional tools for materials discovery, based on serial experiments or first-principles calculations, are slow and expensive. Identifying a means of accelerating the discovery process for materials with exotic electronic spin and charge degrees of freedom is an active area of research [2–10]. In addition, a general approach to design a crystal structure with any desired property, although of great scientific interest and practical importance, is still in the early stages of development [11–13]. The work described here advances the design of novel vdW magnets.

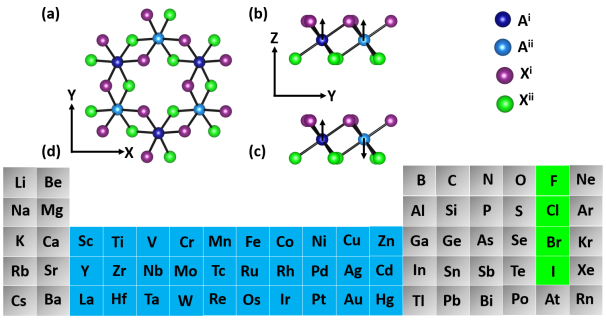

FIG. 1. (a) The crystal structure of the family of transition metal halides A_2X_6, based on Cr_2I_6, used in this study. One or both A sites are replaced with transition metal atoms (highlighted blue in the periodic table in panel (d)) and the X sites (above and/or below) the plane are replaced with halogens (highlighted green). The magnetic configurations studied are (b) ferromagnetic and (c) antiferromagnetic. (d) The elements used to make chemical substitutions are highlighted in the periodic table.

Long-range magnetic ordering in 2D crystals has recently been discovered [14, 15], leading to a race to better understand the properties of magnetism in reduced dimensions and to identify additional 2D magnets with desirable properties for applications in spintronics and data storage [16–19]. Since long-range magnetic order can be strongly suppressed in 2D according to the Mermin-Wagner theorem [20], 2D crystals, such as monolayer CrI_3, provide a new platform for exploring the interplay between reduced dimensionality and magneto-crystalline anisotropy (MCA). MCA stabilizes magnetic ordering in 2D materials. This interplay could give rise to spin degrees of freedom such as spin textures, that have both scientific interest and relevance for developing novel quantum computing architectures.

B. Layered transition metal halides

2D vdW ferromagnets have been identified in five structurally distinct groups, namely, transition metal phosphorous trichalcogenides, transition metal halides, ternary iron-based tellurides, transition metal oxyhalides, and transition metal dichalcogenides [1, 21]. In this study we focus on the family of transition metal halides (see **Figure 1**). This class of 2D solids includes materials with different stoichiometries and crystal phases [22]. They are mainly composed of dihalides MX_2 and trihalides MX_3 (M = V, Cr, Mn, Fe, Co, Ni, Ru; X = Cl, Br, I). Due to the relatively large atomic radius of halide anions and the partially filled 3*d* electronic shells of transition metal cations, magnetic vdW materials with a layered structure are expected to emerge from these compounds [22]. For many years, electronic correlations in Cr trihalides have been investigated, and a series of exciting phenomena were revealed in this family of mate-

[1] This is the pre-peer reviewed version of the following article: T. D. Rhone et al., "Artificial Intelligence Guided Studies of van der Waals Magnets," Adv. Theory Simulations, p. 2300019 (2023), which has been published in final form at https://doi.org/10.1002/adts.202300019. This article may be used for non-commercial purposes in accordance with Wiley Terms and Conditions for Use of Self-Archived Versions.

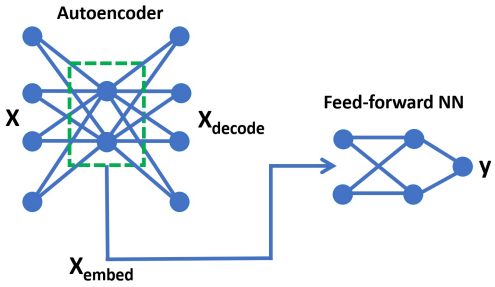

FIG. 2. The neural network architecture used to implement semi-supervised learning. An autoencoder is coupled to a feed-forward neural network. The embedding space of the autoencoder is the input for the feed-forward neural network. The loss functions of the autoencoder and the feed-forward neural network are coupled.

rials. Cr trihalides with different anions exhibit different properties. These include: (a) The intralayer exchange of these three compounds is ferromagnetic (FM), while the interlayer exchange changes from antiferromagnetic (AFM) to FM (from $CrCl_3$ to $CrBr_3$). The magnetic order for CrI_3 depends on the layer number. The corresponding magnetization direction varies from inplane ($CrCl_3$) to out-of-plane ($CrBr_3$ and CrI_3) [23]. (b) Owing to the governing superexchange interaction [24] and spin–orbit coupling (SOC) [24], the Curie temperature T_C of several layers of Cr trihalides increases from 17 K ($CrCl_3$) to 37 K ($CrBr_3$) then to 46 K (CrI_3) [23]; this trend stems from the extended anion radius and as well as higher atomic number. (c) The spin models that describe 2D magnetism are the XY and Ising models for $CrCl_3$ and CrI_3, respectively. The description of $CrBr_3$ lies between the Heisenberg and Ising models [25], indicating the importance of exchange anisotropy linked to the increase of the atomic number of the halide anion. In addition, the spin-flip field decreases with the increasing temperature in CrI_3 and $CrCl_3$ [26]. The T_C of $CrBr_3$ and $CrCl_3$ increases as the magnetic field increases, while it is almost field-independent in CrI_3 due to the large anisotropy. In addition, various phenomena such as large valley splitting [27], higher-spin Kitaev model [28], and quantum anomalous Hall effect [29], have been reported in transition metal halides, suggesting their potentials in different research fields.

Monolayer CrX_3 has a hexagonal lattice with point group D_{3d}. [30] The present study will use this crystal structure as the prototype structure and explore how changes in chemical composition affect its magnetic and thermodynamic properties. A more thorough investigation of competing phases is left for future work.

C. Materials discovery using AI

Materials data (created from experiments or from first-principles calculations) combined with AI can be used to accelerate materials science research and discovery [9, 31–33]. AI models trained on a set of crystal structures and corresponding material properties can predict the properties of a much larger space of materials. In particular, there is a great deal of interest in harnessing AI for identifying novel magnetic materials [8, 9]. Recent studies leveraging AI to study materials highlight the importance of the careful choice of descriptors for making successful predictions [32, 34]. In these studies, state-of-the-art mathematical representations of crystal structures, based on graph neural networks, were constructed to reliably model material properties.

Early efforts to create materials descriptors used chemical composition only [9, 35] and later incorporated simple metrics for encoding crystal structure [36, 37]. Recent studies demonstrate that AI models constructed from descriptors using chemical compositions can be successful if the study is restricted to isostructural materials [9]. Another recent approach of increasing interest is to create mathematical representations of materials from data [32]. AI models (neural networks in particular) are universal function approximators that contain increasingly sophisticated representations in successive hidden layers of the neural network. In the case of the neural network autoencoder architecture, a compressed representation of the data is created in the embedding layer, or latent space of the autoencoder. This gives rise to the prospect of using AI to uncover physical insight through the study of the latent space representation by linking the encoded representation of a material to its target property. The autoencoder's latent space can conceivably elucidate patterns in a high-dimensional descriptor space revealing relationships that lead to physical insight [38].

A major challenge in materials informatics is the scant amount of data, or more specifically, labelled data that can be used for supervised learning. To overcome this challenge, efforts have been made to perform unsupervised learning, where no labels are needed for inference. In addition, semi-supervised learning can be implemented, where both labelled and unlabelled data are exploited to train models [39]. Although the use of semi-supervised learning has already been reported in the materials discovery literature [39], this tool appears to be underutilized by the materials informatics community. Semi-supervised learning can be used to mitigate the challenge of scarce data, since increasing the amount of unlabelled data can improve model performance. Since the bottleneck for training AI models is often the lack of difficult to obtain labelled data, semi-supervised learning provides a significant benefit [39]. In this work, we leverage semi-supervised learning (see **Figure 2**) to overcome the challenge of sparsely labeled data and to search for novel vdW magnets.

TABLE I. DFT identifies candidate materials satisfying the search criteria for the formation energy, E_f [eV] and the magnetic moment, μ [μ_B] of CrI_3. The calculated DFT values for E_f and μ are displayed.

Formula	E_f	μ	Formula	E_f	μ
Cr_2I_6	-6.213	11.3	$Mn_2Cr_2Br_{12}$	-11.082	13.1
$MnCrCl_6$	-15.767	13.1	$MnTcBr_3Cl_3$	-10.971	14.6
$Mn_2I_3Cl_3$	-9.530	15.2	$CrFeCl_6$	-13.650	14.9
$CrFeBr_6$	-9.067	14.8	$MnReI_3Cl_3$	-6.488	14.1
$CrFeI_3Cl_3$	-8.210	14.4	$CrFeBr_3Cl_3$	-11.307	14.9
$Fe_2Br_3Cl_3$	-8.102	18.5			

II. RESULTS AND DISCUSSION

A subset of the density functional theory (DFT) results are shown in **Figure 3**. The displayed results constitute the ground state magnetic configuration, with the formation energy, E_f on the left and the magnetic moment, μ on the right. Calculations were performed on 700 candidates out of a total of $\sim 10^4$ candidates. The grey squares represent the combinations that were not calculated. The magnetic moment and formation energy values vary with changes in chemical composition. The objective in this work is to identify materials with large magnetic moments that are also chemically stable as determined by their formation energy. For instance, we highlight that our

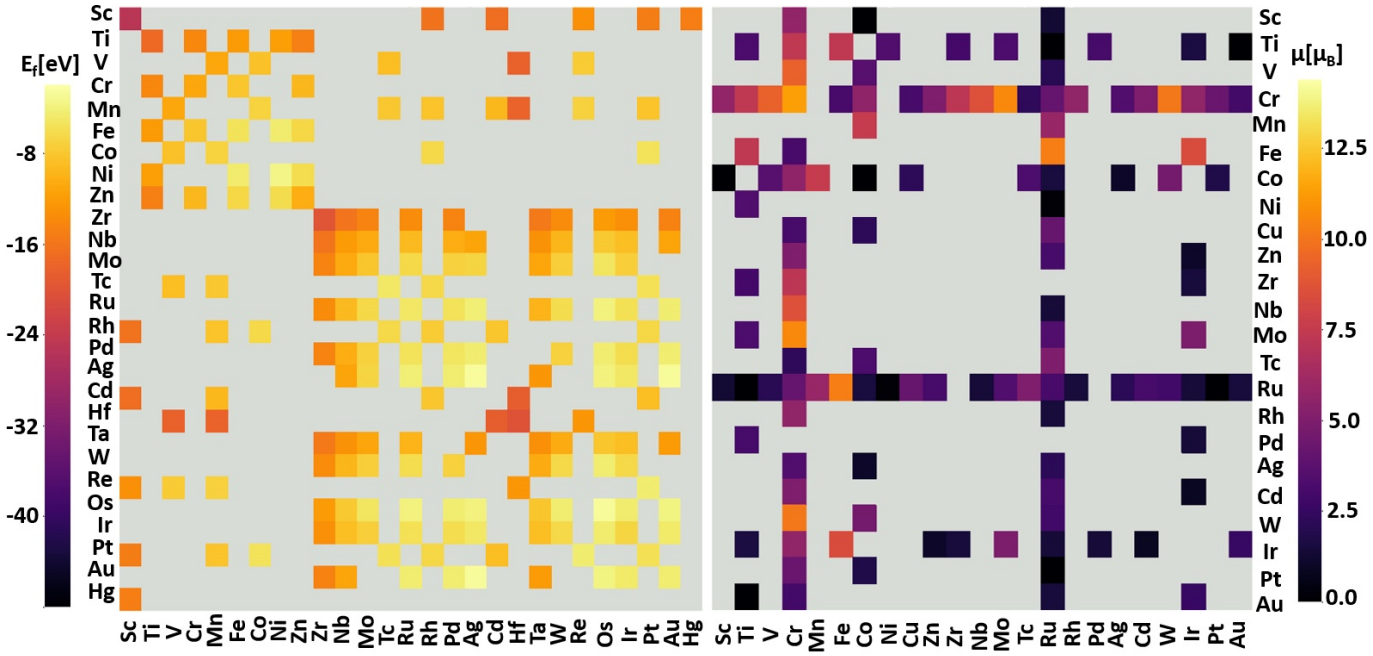

FIG. 3. A subset of the DFT results are displayed. The left panel shows the formation energy, E_f [eV] for $A^iA^{ii}X_3^iX_3^{ii}$ candidates where X^iX^{ii} = Br_3Cl_3. The right panel shows the magnetic moment, μ [μ_B] for $A^iA^{ii}X_3^iX_3^{ii}$ candidates where X^iX^{ii} = I_3I_3. The horizontal axis shows the A^i sites and the vertical axis shows the A^{ii} sites. Candidates that were not calculated are represented by grey squares.

DFT search finds that several A_2X_6 structures have magnetic moments larger than that of CrI_3, with formation energy lower (hence more stable) than that of CrI_3 (see Table I).

Next, we train a NN model to learn the relationship between a crystal structure's chemical composition and its corresponding magnetic and thermodynamic properties. Training was performed with both labeled and unlabeled data using semi-supervised learning. The trained NN facilitates the fast and accurate prediction of materials properties for the entire materials space, allowing us to quickly identify materials candidates that might satisfy our search criteria. The NN model performance is displayed in **Figure 4** for both the magnetic moment and the formation energy. The parity plots show good model performance for both the magnetic moment and the formation energy. We note that the training tasks for the magnetic moment and the formation energy were coupled together and not trained independently using two separate models. An additional training task, the magnetic excitation energy, ΔE, was added to the model's loss function to further constrain the NN. By adding the magnetic excitation energy and the formation energy to the loss function for the magnetic moment prediction, we incorporate soft constraints into the NN. This is an example of physics informed machine learning (PIML), a state-of-the-art approach at the intersection of physics and AI [40–43]. Our PIML approach links the magnetic excitation energy to the physics of the system by mapping the DFT energies to the Heisenberg spin Hamiltonian [44] as shown in Eqn. 1:

$$\begin{aligned} E_{\mathrm{FM}} &= E_0 + (3J_1 + 6J_2 + 3J_3)|\vec{S}|^2) \\ E_{\mathrm{AFM}} &= E_0 + (-3J_1 + 6J_2 - 3J_3)|\vec{S}|^2) \\ \Delta E &= E_{FM} - E_{AFM} \\ &= 6(J_1 + J_3)|\vec{S}^2| \end{aligned} \tag{1}$$

The magnetic excitation energy is the difference in the DFT total energy of the ferromagnetic configurations, E_{FM} and the antiferromagnetic configurations, E_{AFM}. ΔE is determined by J_1 and J_3 (see Equation 1), where J_1, J_2, and J_3 are the first, second and third nearest neighbour interactions respectively. $\vec{S}$ represents the spin on the transition metal atom.

If we require the model to learn ΔE, E_f and μ simultaneously, we can better constrain the NN model. We find that this soft constraint decreases overfitting when compared with a model trained with only μ in the loss function.

To demonstrate the usefulness of the semi-supervised learning approach we trained several models with varying amounts of unlabelled data. Increasing the amount of unlabelled data increased the NN model performance as shown in **Figure 5**. With about 700 labelled data points and no unlabelled data we obtained an average R^2 validation score of 0.2. With only additional unlabelled data points (up to 4,000) we get an increase in the R^2 to 0.8. The NN performance improves with increased amounts of unlabelled data due to the autoencoder portion of the NN becoming better at learning the materials representation. The FNN is then better able to make predictions given the improved inputs created by the latent space of the autoencoder [45].

We attempt to extract physical insight from the autoencoder NN by analyzing the latent space. Using PCA we project the latent space onto the first two principal components, X_1, X_2 and plot the results in **Figure 6**. A pattern emerges in the 2D projection of the latent space where materials with small magnetic moment are in one region while materials with larger magnetic moments are in another part of the 2D latent space. This suggests that there is a link between crystal structure and chemical composition, as encoded using the SOAP descriptor, and the magnetic moment.

The NN can be used to rapidly predict the properties of candidate materials and to screen for those materials with large magnetic moment and high chemical stability. We compared the AI predictions with the labeled data in the validation/training set; of the 496 predictions, 14 satisfied the following search criterion: magnetic mo-

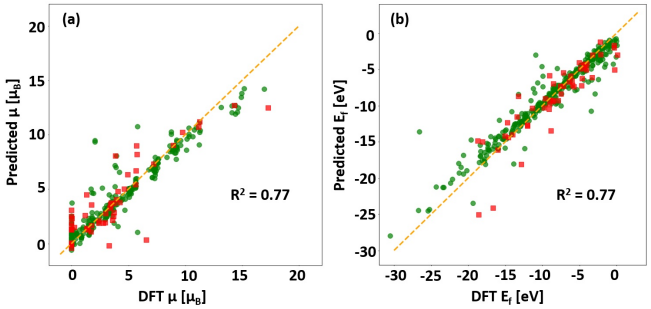

FIG. 4. The parity plot for the AI results are shown for (a) magnetic moment μ [μ_B] and (b) formation energy E_f [eV]. The test set R^2 score is 0.77. The red squares (green circles) indicate test (training) set data.

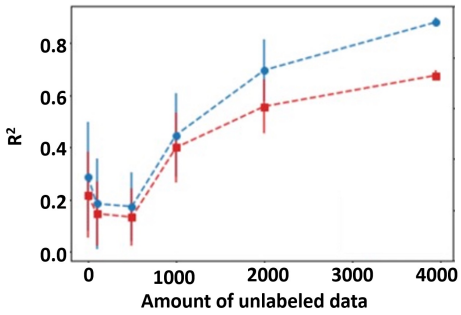

FIG. 5. The R^2 validation set score versus the number of unlabeled data points is displayed. Increasing the amount of unlabeled data in our semi-supervised learning tasks improves the prediction performance. Markers delimit the mean R^2 score and errors bars indicate the standard deviation of these scores for a set of 10 separate runs. The red squares (blue circles) indicate test (training) set data.

ment μ > 11.3 μ_B and formation energy E_f < -6.213 eV. Examples of the promising candidates include: $Mn_4I_6Cl_6$, $Cr_2Fe_2Cl_{12}$ and $Mn_2Cr_2Br_{12}$. The candidates and their corresponding properties are displayed in Table II. Although the formation energy is a proxy for chemical stability, it is a necessary but not sufficient indicator for chemical stability. The absence of imaginary phonon modes gives a more robust estimate of the chemical stability. We calculated the phonon dispersion for the following promising structures: $Cr_2Fe_2Br_6Cl_6$, $Fe_2Cr_2Br_{12}$, $Mn_2Cr_2Cl_{12}$ and $Mn_4I_6Cl_6$ and found that they were dynamically stable except for $Mn_4I_6Cl_6$ [see Supporting Information for further details].

Furthermore, we chose 71 additional candidates at random from the unlabelled data set, predicted their properties using AI and then chose the 6 candidates with the highest magnetic moments with E_f < -6.213 eV. Additional DFT calculations were used to verify the AI predictions. The resulting promising candidates were $CrAuCl_6$, $MnVBr_3Cl_3$, $MnHgBr_3Cl_3$, $MoWBr_3Cl_3$, $MnReBr_3Cl_3$ and $MnCdBr_3Cl_3$. These results along with their corresponding properties are included in Table II.

III. CONCLUSION

We created a machine learning framework leveraging semi-supervised learning to accelerate the discovery of monolayers of transition metal halides. Semi-supervised learning mitigates the lack

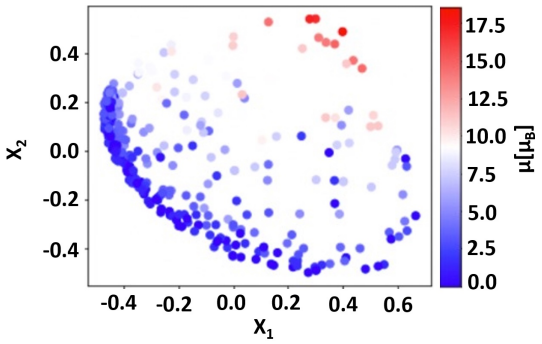

FIG. 6. The two-dimensional projection of the embedding space of the autoencoder neural network is displayed. The first and second principal components, X_1 and X_2, are on the horizontal and vertical axis respectively. A pattern in the data emerges indicating a connection between the position in embedding space and the value of the magnetic moment.

of labelled data by creating a mathematical representation of the materials using unlabelled data. Furthermore, we identified novel transition metal halides with large magnetic moments that are predicted to be chemically stable as evidenced by the thermodynamic and dynamic stability calculations. In particular, we predict that $Cr_2Fe_2Br_6Cl_6$, $Fe_2Cr_2Br_{12}$ and $Mn_2Cr_2Cl_{12}$ are all promising structures with larger magnetic moments and lower formation energy than Cr_2I_6.

Our materials prediction framework can be easily generalized for the exploration of materials with different crystal structures beyond the one considered here. Specifically, different crystal structure prototypes can be used, including mixed ones, for example, a data set comprising both transition metal halides and transition metal trichalcogenides.

IV. EXPERIMENTAL SECTION

1. *Database of first-principles calculations*

In order to create a framework for investigating 2D magnets using a data-driven approach, we first create a database of crystal structures of the form A_2X_6, based on monolayer Cr_2I_6 (**Figure 1(a)**) using DFT calculations with non-collinear spin and spin-orbit interactions included. There is a combinatorially large number of possible candidate A_2X_6 structures ($\sim 10^4$) with different elements occupying the A and X sites. We randomly selected an initial subset of 700 structures for investigation with DFT (and performed calculations on additional structures at a later stage). We obtain the formation energy, magnetic order and magnetic moment of each crystal structure. The ground-state properties were determined by examining the energies of the fully optimized structure with several spin configurations, including parallel, and anti-parallel spin orientations at the A sites (**Figure 1(b)**). The energy difference between parallel and anti-parallel spin configurations estimates the magnetic excitation energy. The sign of the magnetic excitation energy is an indicator of the magnetic order of a material.

To create the database we use DFT calculations with the VASP code [46, 47]. We used the GGA-PBE for the exchange-correlation functional. The energy cutoff was 450 eV. The vacuum region was thicker than 20 Å. Calculations were performed using 2×1 supercells with two A sites per unit cell. The atoms were fully relaxed

TABLE II. Materials candidates that satisfy the search criteria (i.e. higher magnetic moment and lower formation energy than that of Cr_2I_6) are displayed alongside the formation energy, E_f [eV] and the magnetic moment, μ [μ_B] of Cr_2I_6. The calculated DFT values for E_f and μ are displayed alongside the corresponding AI predicted values. The asterisk indicates those candidates initially chosen from the unlabelled data set.

Formula	E_f (DFT)	E_f (AI)	μ (DFT)	μ (AI)
Cr_2I_6	-6.213	-5.8	9.2	11.3
$MnCrBr_6$	-11.082	-11.2	13.1	11.6
$MnCrCl_6$	-15.767	-14.2	13.1	11.7
$MnReI_3Br_3$	-4.397	-6.4	14.1	12.0
$Fe_2Br_3Cl_3$	-8.102	-12.1	18.5	12.0
$CrFeI_3Br_3$	-6.126	-6.8	14.6	12.4
$MnReI_3Cl_3$	-6.489	-7.1	14.1	12.8
$Fe_2I_3Cl_3$	-5.368	-7.4	16.9	13.2
$MnTcBr_3Cl_3$	-10.971	-9.9	14.6	13.5
$CrFeI_3Cl_3$	-8.210	-7.6	14.4	13.5
$CrFeBr_6$	-9.067	-7.8	14.8	13.7
$CrFeCl_6$	-13.651	-12.0	14.9	13.9
$Mn_2I_3Cl_3$	-9.530	-8.3	15.2	14.2
$CrFeBr_3Cl_3$	-11.307	-9.2	14.9	14.3
*$MnCdBr_3Cl_3$	-11.994	-12.8	5.7	6.7
*$MnVBr_3Cl_3$	-14.713	-12.3	11.2	8.1
*$CrAuCl_6$	-8.898	-9.2	8.9	9.4
*$MoWBr_3Cl_3$	-8.568	-6.9	9.8	9.9
*$MnHgBr_3Cl_3$	-9.121	-10.4	5.7	11.1
*$MnReBr_3Cl_3$	-9.643	-9.1	14.3	13.9

until the force on each atom was smaller than $0.01 eV Å^{-1}$. A Γ-centered $8\times8\times1$ k-point mesh was utilized. We create the different structures by choosing different transition metal atoms for each of the Cr atoms in the unit cell. The halogens above and below the basal plane were separately selected from F, Br, Cl, or I. **Figure** 1(d) shows the choice of substitution atoms in the Periodic Table. An example of a structure created through this process is $(CrTi)Br_3Cl_3$. The FM (AFM) configuration was created by making the spins on the A sites parallel (antiparallel). The magnetic moment per supercell and the formation energy per supercell [9] were extracted for each relaxed structure and each magnetic configurations. Dynamic stability was estimated by performing phonon calculations using phonopy [48].

2. *Materials descriptors and AI modelling*

A careful choice of descriptors is essential for the success of any AI approach. Materials descriptors (i.e. mathematical representations of materials) are used for both data analytics and to serve as inputs to AI models. Many materials descriptors have been developed with increasing levels of sophistication, from those based on atomic properties only [35] to those that incorporate clever mathematical descriptions of the crystal structure [36, 37, 49]. In this study we leverage the smooth overlap of atomic orbitals (SOAP) kernel as a descriptor [49]. The SOAP kernel encodes chemical composition and crystal structure into a form that can be cast into a vector that is used to describe the position of materials in chemical space. The SOAP kernel is used as an input for our AI models.

We performed semi-supervised learning using the SOAP kernel as the input and the magnetic moment, the formation energy and the magnetic excitation energy are the target properties. The data were randomly divided into a training/validation set and a test set. Training/validation were typically 90% of the total data while test data comprised 10% of all the data. We employed a combination of neural network (NN) models to perform semi-supervised learning. That is, we coupled an autoencoder with a feed-forward neural network; the autoencoder neural network (ANN) does not require labels (i.e. unsupervised learning) whereas the feed-forward neural network (FNN) requires labels (i.e. supervised learning). See **Figure 2** for a schematic of the architecture. The AENN and FNN models are trained at the same time. Successive layers of the autoencoder network facilitate increasingly higher level materials representations. The optimal number of hidden layers and nodes in each hidden layer was found using random hyperparameter search. The embedding layer (i.e. latent space) of the autoencoder is used as the input to the FNN (see the Supporting Information for details). The embedding layer of the ANN learns a representation of the materials data that can be used for pattern recognition when compressed further into a two-dimensional descriptor space. That is, we can further compress the latent space into two dimensions using principal component analysis (PCA) or t-distributed stochastic neighbor embedding (t-SNE) [50, 51].

Supporting Information

Supporting Information is available from the Wiley Online Library or from the author.

Acknowledgements

This research used resources of the Argonne Leadership Computing Facility, which is a DOE Office of Science User Facility supported under Contract DE-AC02-06CH11357. Calculations were also performed using the Extreme Science and Engineering Discovery Environment (XSEDE), which is supported by National Science Foundation (Grant number ACI-1548562) and the Odyssey cluster supported by the FAS Division of Science, Research Computing Group at Harvard University. This research is supported by the National Science Foundation CAREER award under Grant No 2044842.

Conflict of Interest

The authors declare no conflict of interest.

Data Availability Statement

The data that support the findings of this study are available from the corresponding author upon reasonable request.

[1] Q. H. Wang, A. Bedoya-Pinto, M. Blei, A. H. Dismukes, A. Hamo, S. Jenkins, M. Koperski, Y. Liu, Q.-C. Sun, E. J. Telford, H. H. Kim, M. Augustin, U. Vool, J.-X. Yin, L. H. Li, A. Falin, C. R. Dean, F. Casanova, R. F. L. Evans, M. Chshiev, A. Mishchenko, C. Petrovic, R. He, L. Zhao, A. W. Tsen, B. D. Gerardot, M. Brotons-Gisbert, Z. Guguchia, X. Roy, S. Tongay, Z. Wang, M. Z. Hasan, J. Wrachtrup, A. Yacoby, A. Fert, S. Parkin, K. S. Novoselov, P. Dai, L. Balicas, E. J. G. Santos,

ACS Nano **2022**, *16*, 5 6960.
[2] C. M. Acosta, E. Ogoshi, J. A. Souza, G. M. Dalpian, *ACS Applied Materials & Interfaces* **2022**.
[3] W. Xia, M. Sakurai, B. Balasubramanian, T. Liao, R. Wang, C. Zhang, H. Sun, K.-M. Ho, J. R. Chelikowsky, D. J. Sellmyer, C.-Z. Wang, *Proceedings of the National Academy of Sciences* **2022**, *119*, 47 e2204485119.
[4] S. Haastrup, M. Strange, M. Pandey, T. Deilmann, P. S. Schmidt, N. F. Hinsche, M. N. Gjerding, D. Torelli, P. M. Larsen, A. C. Riis-Jensen, J. Gath, K. W. Jacobsen, J. J. Mortensen, T. Olsen, K. S. Thygesen, *2D Materials* **2018**, *5*, 4 42002.
[5] V. Stanev, K. Choudhary, A. G. Kusne, J. Paglione, I. Takeuchi, *Communications Materials* **2021**, *2*, 1 105.
[6] N. Andrejevic, J. Andrejevic, B. A. Bernevig, N. Regnault, F. Han, G. Fabbris, T. Nguyen, N. C. Drucker, C. H. Rycroft, M. Li, *Advanced Materials* **2022**, *n/a*, n/a 2204113.
[7] H. A. Merker, H. Heiberger, L. Nguyen, T. Liu, Z. Chen, N. Andrejevic, N. C. Drucker, R. Okabe, S. E. Kim, Y. Wang, T. Smidt, M. Li, *iScience* **2022**, *25*, 10 105192.
[8] Y. Xie, G. A. Tritsaris, O. Grånäs, T. D. Rhone, *The Journal of Physical Chemistry Letters* **2021**, 12048–12054.
[9] T. D. Rhone, W. Chen, S. Desai, S. B. Torrisi, D. T. Larson, A. Yacoby, E. Kaxiras, *Scientific Reports* **2020**, *10*, 1 15795.
[10] Y. Zhu, X. Kong, T. D. Rhone, H. Guo, *Phys. Rev. Materials* **2018**, *2*, 8 81001.
[11] C.-T. Chen, G. X. Gu, *Advanced science (Weinheim, Baden-Wurttemberg, Germany)* **2020**, *7*, 5 1902607.
[12] A. Zunger, *Nature Reviews Chemistry* **2018**, *2*, 4 121.
[13] Z. Ren, S. I. P. Tian, J. Noh, F. Oviedo, G. Xing, J. Li, Q. Liang, R. Zhu, A. G. Aberle, S. Sun, X. Wang, Y. Liu, Q. Li, S. Jayavelu, K. Hippalgaonkar, Y. Jung, T. Buonassisi, *Matter* **2022**, *5*, 1 314.
[14] B. Huang, G. Clark, E. Navarro-Moratalla, D. R. Klein, R. Cheng, K. L. Seyler, D. Zhong, E. Schmidgall, M. A. McGuire, D. H. Cobden, W. Yao, D. Xiao, P. Jarillo-Herrero, X. Xu, *Nature* **2017**, *546*, 7657 270.
[15] C. Gong, L. Li, Z. Li, H. Ji, A. Stern, Y. Xia, T. Cao, W. Bao, C. Wang, Y. Wang, Z. Q. Qiu, R. J. Cava, S. G. Louie, J. Xia, X. Zhang, *Nature* **2017**, *546*, 7657 265.
[16] N. S. Kiselev, A. N. Bogdanov, R. Schäfer, U. K. Rößler, *Journal of Physics D: Applied Physics* **2011**, *44*, 39 392001.
[17] W. Han, *APL Mater.* **2016**, *4*, 3 32401.
[18] A. Hirohata, K. Yamada, Y. Nakatani, I.-L. Prejbeanu, B. Diény, P. Pirro, B. Hillebrands, *Journal of Magnetism and Magnetic Materials* **2020**, *509* 166711.
[19] H. Y. Yuan, Y. Cao, A. Kamra, R. A. Duine, P. Yan, *Physics Reports* **2022**, *965* 1.
[20] N. D. Mermin, H. Wagner, *Phys. Rev. Lett.* **1966**, *17*, 22 1133.
[21] X. Jiang, Q. Liu, J. Xing, N. Liu, Y. Guo, Z. Liu, J. Zhao, *Applied Physics Reviews* **2021**, *8*, 3 31305.
[22] M. McGuire, *Crystals* **2017**, *7*, 5 121.
[23] H. H. Kim, B. Yang, S. Li, S. Jiang, C. Jin, Z. Tao, G. Nichols, F. Sfigakis, S. Zhong, C. Li, S. Tian, D. G. Cory, G.-X. Miao, J. Shan, K. F. Mak, H. Lei, K. Sun, L. Zhao, A. W. Tsen, *Proceedings of the National Academy of Sciences* **2019**, *116*, 23 11131.
[24] D.-H. Kim, K. Kim, K.-T. Ko, J. Seo, J. S. Kim, T.-H. Jang, Y. Kim, J.-Y. Kim, S.-W. Cheong, J.-H. Park, *Phys. Rev. Lett.* **2019**, *122* 207201.
[25] C. Jin, Z. Tao, K. Kang, K. Watanabe, T. Taniguchi, K. F. Mak, J. Shan, *Nature Materials* **2020**, *19*, 12 1290.
[26] H. H. Kim, B. Yang, S. Tian, C. Li, G.-X. Miao, H. Lei, A. W. Tsen, *Nano Letters* **2019**, *19*, 8 5739, pMID: 31305077.
[27] Q. Li, K.-Q. Chen, L.-M. Tang, *Phys. Rev. Applied* **2020**, *13* 014064.
[28] P. P. Stavropoulos, D. Pereira, H.-Y. Kee, *Phys. Rev. Lett.* **2019**, *123* 037203.
[29] J. Sun, X. Zhong, W. Cui, J. Shi, J. Hao, M. Xu, Y. Li, *Phys. Chem. Chem. Phys.* **2020**, *22* 2429.
[30] M. A. McGuire, H. Dixit, V. R. Cooper, B. C. Sales, *Chem. Mater.* **2015**, *27* 612.
[31] F. Mayr, M. Harth, I. Kouroudis, M. Rinderle, A. Gagliardi, *Journal of Physical Chemistry Letters* **2022**, *13*, 8 1940.
[32] J. Noh, J. Kim, H. S. Stein, B. Sanchez-Lengeling, J. M. Gregoire, A. Aspuru-Guzik, Y. Jung, *Matter* **2019**, *1*, 5 1370.
[33] T. Ueno, T. D. Rhone, Z. Hou, T. Mizoguchi, K. Tsuda, *Materials Discovery* **2016**, *4* 18.
[34] R. E. A. Goodall, A. A. Lee, *Nature Communications* **2020**, *11*, 1 6280.
[35] L. M. Ghiringhelli, J. Vybiral, S. V. Levchenko, C. Draxl, M. Scheffler, *Phys. Rev. Lett.* **2015**, *114*, 10 105503.
[36] M. Rupp, A. Tkatchenko, K.-R. Müller, O. A. von Lilienfeld, *Phys. Rev. Lett.* **2012**, *108*, 5 58301.
[37] K. Hansen, F. Biegler, R. Ramakrishnan, W. Pronobis, O. A. von Lilienfeld, K.-R. Müller, A. Tkatchenko, *The Journal of Physical Chemistry Letters* **2015**, *6*, 12 2326.
[38] F. Oviedo, J. L. Ferres, T. Buonassisi, K. T. Butler, *Accounts of Materials Research* **2022**, *3*, 6 597.
[39] N. C. Frey, J. Wang, G. I. Vega Bellido, B. Anasori, Y. Gogotsi, V. B. Shenoy, *ACS Nano* **2019**, *13*, 3 3031.
[40] G. E. Karniadakis, I. G. Kevrekidis, L. Lu, P. Perdikaris, S. Wang, L. Yang, *Nature Reviews Physics* **2021**, *3*, 6 422.
[41] V. Fung, P. Ganesh, B. G. Sumpter, *Chemistry of Materials* **2022**, *34*, 11 4848.
[42] M. Mattheakis, D. Sondak, A. S. Dogra, P. Protopapas, *Physical Review E* **2022**, *105*, 6.
[43] G. P. P. Pun, R. Batra, R. Ramprasad, Y. Mishin, *Nature Communications* **2019**, *10*, 1 2339.
[44] N. Sivadas, M. W. Daniels, R. H. Swendsen, S. Okamoto, D. Xiao, *Phys. Rev. B* **2015**, *91*, 23 235425.
[45] L. Wang, S. Tao, P. Zhu, W. Chen, *Journal of Mechanical Design* **2020**, *143*, 3.
[46] G. Kresse, J. Hafner, *Phys. Rev. B* **1993**, *47*, 1 558.
[47] G. Kresse, J. Furthmüller, *Computational Materials Science* **1996**, *6*, 1 15.
[48] A. Togo, I. Tanaka, *Scr. Mater.* **2015**, *108* 1.
[49] A. P. Bartók, R. Kondor, G. Csányi, *Phys. Rev. B* **2013**, *87*, 18 184115.
[50] R. Tibshirani, G. James, D. Witten, T. Hastie, An introduction to statistical learning-with applications in R, **2013**.
[51] A. Gisbrecht, A. Schulz, B. Hammer, *Neurocomputing* **2015**, *147* 71.